Role of axial mass and strange axial form factor from various target nuclei in neutrino-nucleus scattering

K. S. Kim* and Ki-Seok Choi
School of Liberal Arts and Science, Korea Aerospace University, Koyang 412-791, Korea

Myung-Ki Cheoun
Department of Physics, Soongsil University, Seoul 156-743, Korea

W. Y. So
Department of Radiological Science, Kangwon National University, Samcheok 245-711, Korea

Heejang Moon
School of Aerospace and Mechanical Engineering, Korea Aerospace University, Koyang 412-791, Korea

(Received 6 July 2018; revised manuscript received 15 July 2019; published 4 September 2019)

The roles of strange axial form factor and axial mass for both neutral-current and charged-current reactions are investigated in the quasi-elastic neutrino-nucleus scattering within a relativistic single-particle model. The calculation is performed for various target nuclei like ^{12}C, ^{40}Ca, ^{56}Fe, and ^{208}Pb at the incident neutrino (antineutrino) energies of 1.0 and 2.0 GeV. Then we discuss the dependence of differential cross section on the role of axial mass and strange axial form factor with different target nuclei on both neutral-current and charged-current reactions. Finally we compare our results with the MiniBooNE, T2K, and MINERνA experimental data for the double-differential cross section and the scaled total cross section.

DOI: 10.1103/PhysRevC.100.034604

I. INTRODUCTION

Neutrino-nucleus (ν-A) scattering experiments have been recently performed at several laboratories [1–8]. These neutrino experiments provide high-precision measurements of differential cross sections from various target nuclei. In particular, quasi-elastic ν-A scattering is one of tools used to study several fields of physics for accelerator-based oscillation experiments, but this requires models for neutrino kinematics, target nucleus, and electroweak current operator. The neutrino flux is used by averaging energy as the neutrino beam due to detecting the neutrino, and the relativistic mean field (RMF), the random-phase approximation (RPA), the Fermi gas, or so on are used to model the target nucleus. The electroweak current operator is composed of two vectors, $F_{1,2}(Q^2)$, one axial vector, $G_A(Q^2)$, and one pseudoscalar, $G_P(Q^2)$. In this operator, there are some ambiguities for the strange axial form factor and axial mass in the axial form factor.

From the measurement of the flux-averaged differential cross section at the MiniBooNE experiment [2], new values of axial mass (M_A) and strange axial form factor (g_A^s) from the neutral-current (NC) reaction were extracted at four-momentum transfer squared, $Q^2 = 0$, which are $M_A = 1.39 \pm 0.11$ GeV and $g_A^s = 0.08 \pm 0.26$. The other value of M_A was measured to be $1.23^{+0.13}_{-0.09}$ GeV at the MINOS experiment [9] in the charged-current (CC) quasi-elastic scattering from ^{56}Fe and was also measured to be $1.26^{+0.21}_{-0.18}$ GeV at the T2K experiment [10] from ^{12}C. Another value of M_A was measured to be 0.99 GeV by the MINERνA Collaboration [5], which is in good agreement with standard value, 1.032 GeV.

There have been many theoretical works [11–19] for the axial strange form factor and the nonstandard axial mass. Reference [11] calculated the NC quasi-elastic cross section with the relativistic Green's function method, and the results describe the experimental data with the standard value of the nucleon M_A and also studied the role of g_A^s, which hardly affect the cross section. Butkevich and Perevalov [12] obtained the $g_A^s = -0.11$ by using the MiniBooNE data in the high-energy region with the relativistic distorted-wave impulse approximation (RDWIA), and also extracted $M_A = 1.37$ GeV with the RDWIA and $M_A = 1.36$ GeV by using a relativistic Fermi gas model (RFGM). The authors of Ref. [13] calculated the ν-^{12}C cross section associated with MiniBooNE data by including the multinucleon (np-nh) contribution. In Ref. [14], the CC double cross section was calculated including two-nucleon processes and π- production, and then they compared their results with the MiniBooNE data by scaling $M_A = 1.03$ GeV to $M_A = 1.35$ GeV with the underestimation of the neutrino flux. Moreover, the authors of Ref. [15] calculated the CC double cross section with multinucleon processes and extracted $M_A = 1.08 \pm 0.03$ GeV with a global normalization scale value, $\lambda = 0.92 \pm 0.03$. That is, these papers argued that

*kyungsik@kau.ac.kr

the standard axial mass could explain the MiniBooNE data with the contribution from multinucleon excitations like the 2p-2h contribution.

The NC cross section [16] was calculated within two nuclear models: the superscaling (SuSA) model and the RMF model. The value of the M_A was 1.34 ± 0.06 GeV for RMF and was 1.42 ± 0.06 GeV for SuSA, and that of g_A^s was 0.04 ± 0.28 for RMF and -0.06 ± 0.31 for SuSA. Another value of M_A [17] was extracted as about $M_A = 0.84^{+0.12}_{-0.04} \pm 0.11$ GeV in the range of $Q^2 = 0.1$–1.0 $(\mathrm{GeV}/c)^2$ using the antineutrino CC scattering data from MiniBooNE [3]. The Granada group [18] studied the role of g_A^s by using an axial-vector-meson-dominance model, and the most sensitive region in the MiniBooNE data is in the range $0.2 \lesssim Q^2 \lesssim 0.6$ $(\mathrm{GeV}/c)^2$. They also investigated the effect of the functional form of the axial form factor providing meson dominance and proper perturbative QCD. The 2p-2h meson-exchange currents in Ref. [19] were evaluated on the CC ν-A scattering through the analysis of 2p-2h axial and vector contributions in a relativistic Fermi gas model.

In our previous paper [20], we studied the effect of g_A^s on the cross section, the asymmetry, and the ratio of NC to CC reactions and as the result, the effect appears to be on the asymmetry and the ratio although it is very small on the corresponding cross sections. Recently, we investigated the influence of both M_A and g_A^s on the cross section, the separated cross sections associated with the longitudinal and transverse response functions, the asymmetry, and the various ratios of NC to CC reactions [21].

On the other hand, there are some works [22,23] on other functional forms of the axial form factor of nucleon. The axial form factor in Ref. [22] was studied in a two-component model consisting of a three-quark structure surrounded by a meson cloud and the axial form factor extracted from the experimental data in the spacelike region are model dependent. In Ref. [23], the axial form factor was extracted from neutrino-deuteron scattering data by using the Bayesian approach for feed-forward neural networks and then the corrections from the deuteron structure play a crucial role at the low-Q^2 region ($0.05 < Q^2 < 0.10$ GeV^2).

Furthermore, it is worth studying the relevance of the different nuclear targets for current and forthcoming neutrino oscillation experiments as well as the potential of the RMF to model asymmetric nuclear targets in neutrino experiments due to its realistic separation into proton and neutron contributions. In this work, we investigate the effects of M_A and g_A^s by calculating the inclusive NC and CC reactions in the $\nu(\bar{\nu})$-A scattering from various target nuclei such as ^{12}C, ^{40}Ca, ^{56}Fe, and ^{208}Pb. In particular, since ^{56}Fe is an asymmetric target because of its differing numbers of protons and neutrons, we may obtain interesting information regarding the difference between proton and neutron by separately detecting knockout protons and neutrons. To do these calculations, a relativistic single-particle model is used for bound and continuum nucleons. The bound nucleon wave functions are generated by solving the Dirac equation in the presence of the scalar and vector potential based on the σ-ω model [24]. The wave functions of the continuum nucleon are obtained by the same potential of the bound nucleons, called the RMF. This RMF model guarantees the current conservation and gauge invariance and provides very good agreement [25,26] with (e, e') Bates and SLAC experimental data with the inclusion of the Coulomb distortion for the incoming and outgoing electrons [27]. This approach based on the RMF may help us to analyze not only the lepton kinematics but also hadron kinematics, which has been used in the electron-scattering analysis in ν-A scattering, as recently done in the MINERvA [28] and T2K experiments [29].

The outline of this paper is as follows: In Sec. II we present briefly the formalism for the NC and CC reactions, in Sec. III the results are presented, and finally the summary and conclusion are given in Sec. IV.

II. FORMALISM

To calculate the $\nu(\bar{\nu})$-A scattering, we use the laboratory coordinate system where the target nucleus is at the origin of the coordinate system. The four-momenta of the incident and outgoing neutrinos (antineutrinos) are labeled $p_i^\mu = (E_i, \mathbf{p}_i)$ and $p_f^\mu = (E_f, \mathbf{p}_f)$. $p_A^\mu = (E_A, \mathbf{p}_A)$, $p_{A-1}^\mu = (E_{A-1}, \mathbf{p}_{A-1})$, and $p^\mu = (E_N, \mathbf{p})$ represent the four-momenta of the target nucleus, the residual nucleus, and the knocked-out nucleon, respectively. For the NC and CC reactions, the inclusive cross section, where the outgoing lepton is not detected, is given by the contraction between lepton and hadron tensor:

$$\frac{d\sigma}{dT_N} = 4\pi^2 \frac{M_N M_{A-1}}{(2\pi)^3 M_A} \int \sin\theta_l d\theta_l \int \sin\theta_N d\theta_N p f_{\mathrm{rec}}^{-1} \sigma_M^{Z,\,W^\pm} \times [v_L R_L + v_T R_T + h v_T' R_T'], \tag{1}$$

where θ_l denotes the scattering angle of the lepton, θ_N is the polar angle of the knocked-out nucleons, and $h = -1 (h = +1)$ corresponds to the intrinsic helicity of the incident neutrino (antineutrino). R_L, R_T, and R_T' are the longitudinal, transverse, and transverse interference response functions, respectively. Detailed forms for the kinematical coefficients v and the corresponding response functions R for $\nu(\bar{\nu})$-A scattering are given in Refs. [20,30]. The squared four-momentum transfer is given by $Q^2 = q^2 - \omega^2 = -q_\mu^2$. For the NC reaction, the kinematic factor σ_M^Z is defined by

$$\sigma_M^Z = \left(\frac{G_F \cos(\theta_l/2) E_f M_Z^2}{\sqrt{2}\pi \left(Q^2 + M_Z^2\right)} \right)^2, \tag{2}$$

and for the CC reaction

$$\sigma_M^{W^\pm} = \sqrt{1 - \frac{M_l^2}{E_f}} \left(\frac{G_F \cos(\theta_C) E_f M_W^2}{2\pi \left(Q^2 + M_W^2\right)} \right)^2, \tag{3}$$

where M_Z and M_W are the rest mass of the Z boson and W boson, respectively. θ_C represents the Cabibbo angle given by $\cos^2\theta_C \simeq 0.9749$. G_F denotes the Fermi constant. The recoil factor f_{rec} is written as

$$f_{\mathrm{rec}} = \frac{E_{A-1}}{M_A} \left| 1 + \frac{E_p}{E_{A-1}} \left[1 - \frac{\mathbf{q} \cdot \mathbf{p}}{p^2} \right] \right|. \tag{4}$$

The weak current J^μ represents the Fourier transform of the nucleon current density and is written as

$$J^\mu = \int \bar{\psi}_p \hat{\mathbf{J}}^\mu \psi_b e^{i\mathbf{q}\cdot\mathbf{r}} d^3r, \tag{5}$$

where $\hat{\mathbf{J}}^\mu$ is a free weak nucleon current operator, and ψ_p and ψ_b are wave functions of the knocked-out nucleon and the bound-state nucleon, respectively. For a free nucleon, the current operator comprises the weak vector and the axial-vector form factors:

$$\hat{\mathbf{J}}^\mu = F_1^V(Q^2)\gamma^\mu + F_2^V(Q^2)\frac{i}{2M_N}\sigma^{\mu\nu}q_\nu + G_A(Q^2)\gamma^\mu\gamma^5 + \frac{1}{2M_N}G_P(Q^2)q^\mu\gamma^5, \tag{6}$$

where M_N denotes the mass of the nucleon. By the conservation of the vector current (CVC) hypothesis, the vector form factors for the proton (neutron), $F_i^{V,\,p(n)}(Q^2)$, are expressed as

$$\begin{aligned} F_i^{V,\,p(n)}(Q^2) &= \left(\tfrac{1}{2} - 2\sin^2\theta_W\right)F_i^{p(n)}(Q^2) \\ &\quad - \tfrac{1}{2}F_i^{n(p)}(Q^2) - \tfrac{1}{2}F_i^s(Q^2) \text{ for the NC,} \\ F_i^V(Q^2) &= F_i^p(Q^2) - F_i^n(Q^2) \text{ for the CC,} \end{aligned} \tag{7}$$

where θ_W is the Weinberg angle given by $\sin^2\theta_W = 0.2224$.

The strange vector form factor $F_i^s(Q^2)$ in Eq. (7) are usually given as a dipole form, independently of the nucleon isospin:

$$\begin{aligned} F_1^s(Q^2) &= \frac{F_1^s(0)Q^2}{(1+\tau)\left(1+Q^2/M_V^2\right)^2}, \\ F_2^s(Q^2) &= \frac{F_2^s(0)}{(1+\tau)\left(1+Q^2/M_V^2\right)^2}, \end{aligned} \tag{8}$$

where $\tau = Q^2/(4M_N^2)$ and $M_V = 0.843$ GeV is the cutoff mass parameter usually adopted for nucleon electromagnetic form factors. $F_1^s(0)$ is defined as the squared strange radius of the nucleus, $F_1^s(0) = dG_E^s(Q^2)/dQ^2|_{Q^2=0} = 0.53$ GeV^{-2}, and $F_2^s(0) = \mu_s = -0.4$ is an anomalous strange magnetic moment.

The axial form factors are given by

$$G_A(Q^2) = \tfrac{1}{2}\left(\mp g_A + g_A^s\right)/\left(1+Q^2/M_A^2\right)^2, \tag{9}$$

where $g_A = 1.262$, $M_A = 1.032$ GeV, and $g_A^s = -0.19$, which represents the strange quark contents on the nucleon. The sign $-$ $(+)$ coming from the isospin dependence denotes the knocked-out proton (neutron), respectively.

The induced pseudoscalar form factor is parametrized by the Goldberger-Treimann relation

$$G_P(Q^2) = \frac{2M_N}{Q^2+m_\pi^2}G_A(Q^2), \tag{10}$$

where m_π is the pion mass. But the contribution of the pseudoscalar form factor vanishes for the NC reaction because of the negligible final lepton mass participating in this reaction.

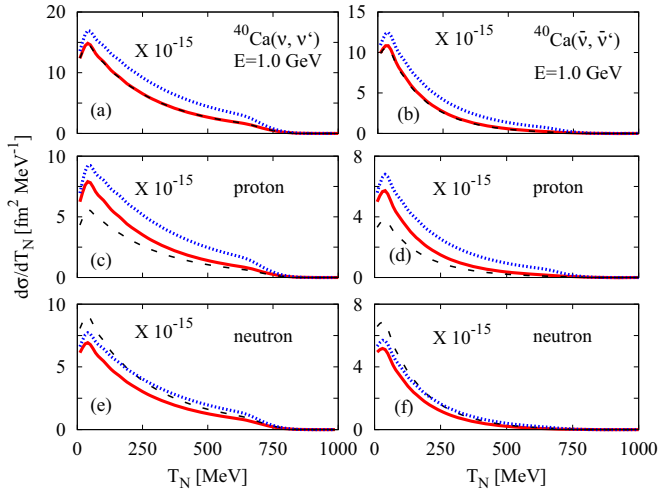

FIG. 1. Differential cross sections of the NC ν-A scattering in terms of the kinetic energy of the knocked-out nucleon for incident neutrino (left panels) and antineutrino (right panels) energy of 1.0 GeV from ^{40}Ca. Solid (red) curves are the results for $M_A = 1.032$ GeV and $g_A^s = -0.19$, dashed (black) curves are for $M_A = 1.032$ GeV and $g_A^s = 0.08$, and dotted (blue) curves are for $M_A = 1.39$ GeV and $g_A^s = -0.19$. The second and third panels from the top are the results for only protons and neutrons in the target nucleus participating the reaction, respectively.

III. RESULTS

We study the effects of the axial mass and the strange form factor in the NC and CC reactions for the $\nu(\bar{\nu})$-A scattering from various target nuclei like ^{12}C, ^{40}Ca, ^{56}Fe, and ^{208}Pb within the framework of a relativistic single-particle model.

In Fig. 1, we calculate the differential cross sections for the NC reaction in terms of the kinetic energies of the knocked-out nucleons from ^{40}Ca at the incident neutrino energy 1.0 GeV. The left panels are the results for the incident neutrino and the right panels are for the incident antineutrino.

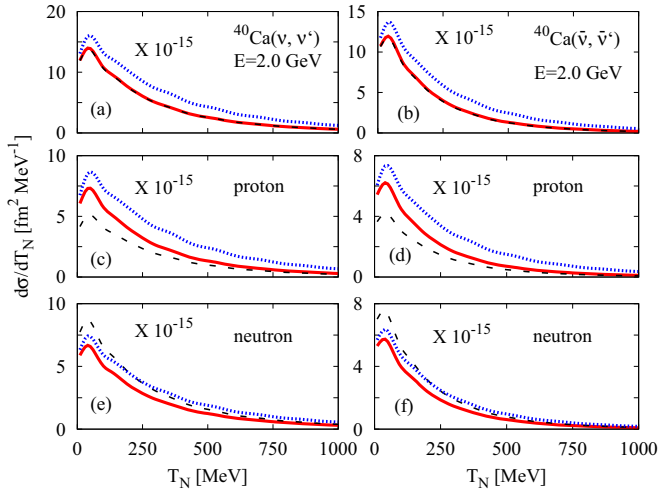

FIG. 2. The same as in Fig. 1 but for an incident neutrino (antineutrino) energy of 2.0 GeV.

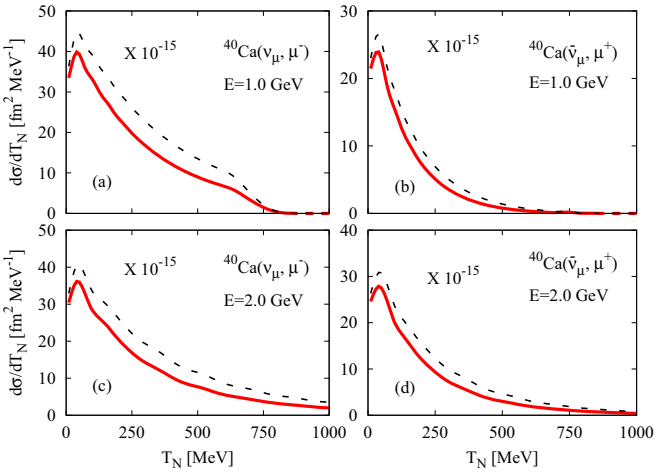

FIG. 3. Differential cross sections of the CC ν-A scattering in terms of the kinetic energy of the knocked-out nucleon for the incident neutrino energies of 1.0 GeV and 2.0 GeV from ^{40}Ca. Solid (red) curves are the results for $M_A = 1.032$ GeV and dashed (black) curves are for $M_A = 1.39$ GeV. The left panels are the results for the neutrino and the right panels are for the antineutrino.

Solid (red) curves are the results for $M_A = 1.032$ GeV and $g_A^s = -0.19$, dashed (black) curves are for $M_A = 1.032$ GeV and $g_A^s = 0.08$, and dotted (blue) curves are for $M_A = 1.39$ GeV and $g_A^s = -0.19$. The first panel [Figs. 1(a) and 1(b)] shows the results of the summation of all nucleons participating in the reaction from a target nucleus. The second and third panels from the top are the results for proton knockout [Figs. 1(c) and 1(d)] and neutron knockout [Figs. 1(e) and 1(f)] in the target nucleus participating the reaction, respectively.

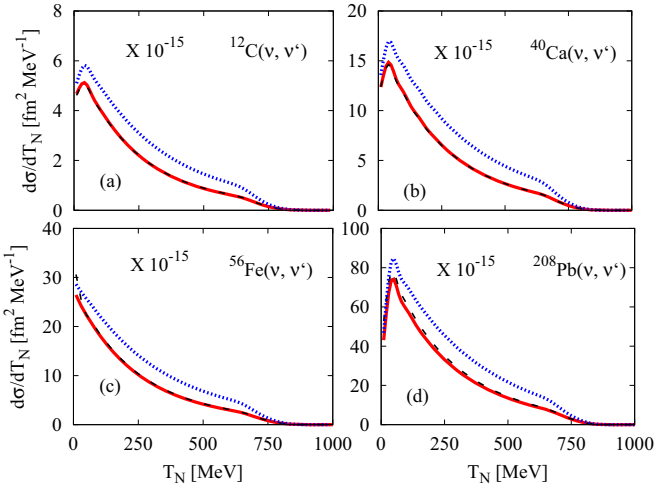

FIG. 4. Differential cross sections of the NC ν-A scattering in terms of the kinetic energy of the knocked-out nucleon for an incident neutrino energy of 1.0 GeV from ^{12}C, ^{40}Ca, ^{56}Fe, and ^{208}Pb. Solid (red) curves are the results for $M_A = 1.032$ GeV and $g_A^s = -0.19$, dashed (black) curves are for $M_A = 1.032$ GeV and $g_A^s = 0.08$, and dotted (blue) curves are for $M_A = 1.39$ GeV and $g_A^s = -0.19$.

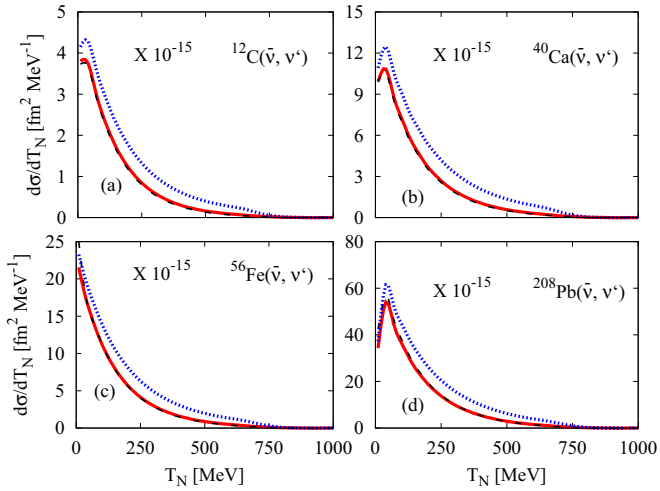

FIG. 5. The same as in Fig. 4 but for an incident antineutrino.

Around the peak, the role of g_A^s reduces the cross section for proton knockout by about 42% but enhances it for neutron knockout by about 30% for the incident neutrino, and for the antineutrino decreases it by about 40% for proton knockout but increases it by about 32% for neutron knockout because of the sign in Eq. (9). The g_A^s contribution reduces the sum of the cross section by about 1.5% for the incident neutrino and by about 2.5% for the antineutrino because it cancels out for proton knockout and neutron knockout. The increase of M_A enhances the cross sections for proton knockout by about 17% and for neutron knockout by about 11%, and consequently the contribution of M_A enhances the sum of the differential cross section by about 15%. Note that the contribution of M_A is almost the same for both incident-neutrino and -antineutrino

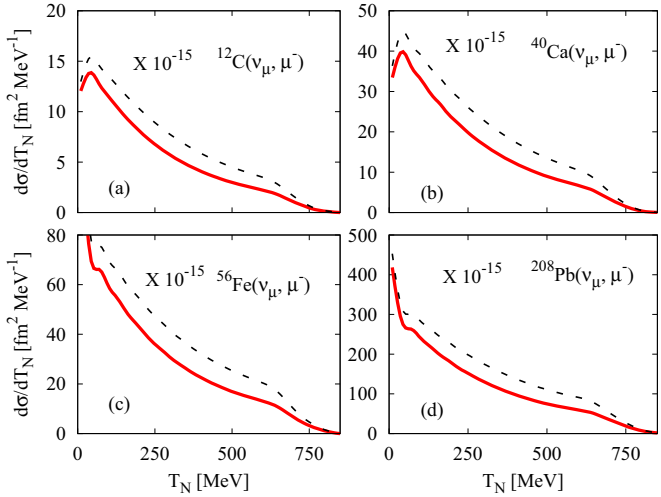

FIG. 6. Differential cross sections of the CC ν-A scattering in terms of the kinetic energy of the knocked-out nucleon for an incident neutrino energy of 1.0 GeV from ^{12}C, ^{40}Ca, ^{56}Fe, and ^{208}Pb. Solid (red) curves are the results for $M_A = 1.032$ GeV and dashed (black) curves are for $M_A = 1.39$ GeV.

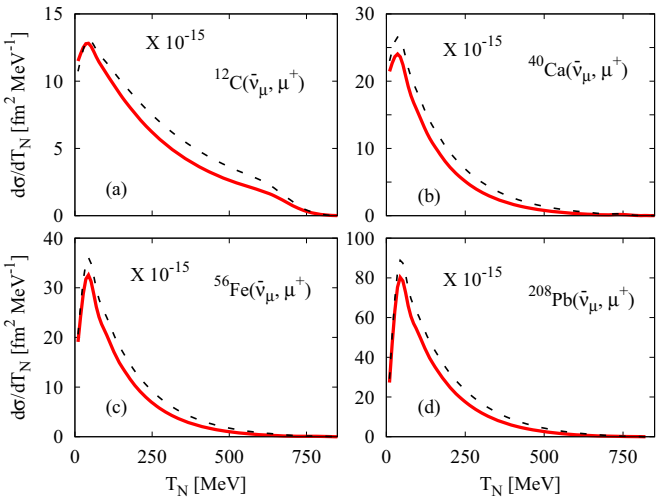

FIG. 7. The same as in Fig. 6 but for an incident antineutrino.

cases. From these results, the sensitivity of proton knockout is slightly higher for the role of both g_A^s and M_A.

Figure 2 shows the cross sections of the incident neutrino energy 2.0 GeV, and the kinematics are the same as in Fig. 1. The shapes are similar to those of Fig. 1 but the magnitude of the cross sections is slightly smaller than that for the case of an energy of 1.0 GeV. As shown in Fig. 1, the role of g_A^s with the incident neutrino reduces the cross section for proton knockout by about 44% but enhances it for neutron knockout by about 30%, and with the antineutrino decreases it by about 48% for proton knockout but increases it by about 31% for neutron knockout. The effect of g_A^s reduces the sum of the cross section by about 1.5% for the incident neutrino and by about 2.0% for the antineutrino. The increase in M_A enhances the cross sections for proton knockout by about 17% and for neutron knockout by about 11%, and as a result the effect of M_A enhances the differential cross section by about 14%. From the results of Figs. 1 and 2, the role of g_A^s and M_A is less sensitive to incident neutrino (antineutrino) energies.

In Fig. 3, we calculate the differential cross sections for the CC reaction in terms of the kinetic energies of the knocked-out nucleons from ^{40}Ca at the incident neutrino (antineutrino) energies of 1.0 and 2.0 GeV. The left panels show the results for an incident neutrino and the right panels are for an incident antineutrino. Solid (red) curves are the results for $M_A =$ 1.032 GeV and dashed (black) curves are for $M_A = 1.39$ GeV. Around the peak, the effect of M_A enhances the cross sections for the neutrino by about 12% and for the antineutrino by about 11% for the two incident energies of 1.0 and 2.0 GeV.

TABLE I. The changing ratios of g_A^s by switching -0.19 to 0.08 around the peak position. The ratios are decreasing percentages for ^{12}C and ^{40}Ca, and are increasing percentages for ^{56}Fe and ^{208}Pb.

g_A^s	^{12}C	^{40}Ca	^{56}Fe	^{208}Pb
(ν, ν')	1.0%	1.5%	1.5%	5.0%
$(\bar{\nu}, \bar{\nu}')$	2.0%	3.0%	1.0%	5.0%

TABLE II. The increasing percentages of M_A by switching 1.032 GeV to 1.39 GeV around the peak position.

M_A	^{12}C	^{40}Ca	^{56}Fe	^{208}Pb
(ν, ν')	14%	14%	17%	17%
$(\bar{\nu}, \bar{\nu}')$	14%	15%	14%	14%
(ν_μ, μ^-)	12%	12%	15%	15%
$(\bar{\nu}_\mu, \mu^+)$	5%	11%	11%	11%

Like the result of the NC reaction, the contribution of M_A does not depend on the incident neutrino (antineutrino) energies.

As shown in Fig. 4, we calculate the differential cross sections for the NC reaction in terms of the kinetic energies of the knocked-out nucleons from ^{12}C, ^{40}Ca, ^{56}Fe, and ^{208}Pb at the incident neutrino energy 1.0 GeV. Solid (red) curves are the results for $M_A = 1.032$ GeV and $g_A^s = -0.19$, dashed (black) curves are for $M_A = 1.032$ GeV and $g_A^s = 0.08$, and dotted (blue) curves are for $M_A = 1.39$ GeV and $g_A^s = -0.19$. The effect of g_A^s reduces the cross section by about 1.0% for ^{12}C and by about 1.5% for ^{40}Ca but enhances it by about 1.5% for ^{56}Fe and by about 5.0% for ^{208}Pb. While the effect of g_A^s reduces the cross sections for ^{12}C and ^{40}Ca, it enhances the cross sections for ^{56}Fe and ^{208}Pb because the number of protons and neutrons is the same for ^{12}C and ^{40}Ca but for ^{56}Fe and ^{208}Pb the number of neutrons is more than number of protons. Note that the effect of M_A enhances the cross sections by about 14% from ^{12}C and ^{40}Ca and by about 17% from ^{56}Fe and ^{208}Pb.

Figure 5 shows the cross sections of the incident antineutrino, and the kinematics are the same as in Fig. 4. The effect of g_A^s reduces the cross section by about 2.0% for ^{12}C and by about 3.0% for ^{40}Ca but enhances it by about 1.0% for ^{56}Fe and by about 5.0% for ^{208}Pb. The effect of M_A enhances the

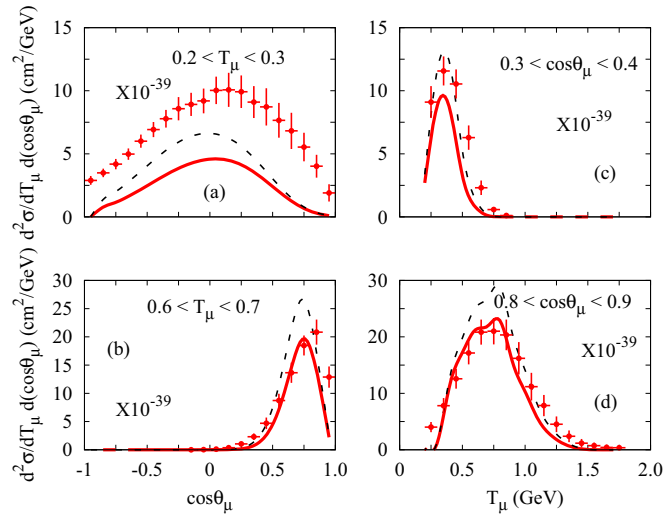

FIG. 8. Double-differential cross sections of CC ν-A scattering in terms of the kinetic energy and the scattering angle of the outgoing muon from ^{12}C. Solid (red) curves are the results for $M_A =$ 1.032 GeV, dashed (black) curves are for $M_A = 1.39$ GeV, and the data were measured from the MiniBooNE [1].

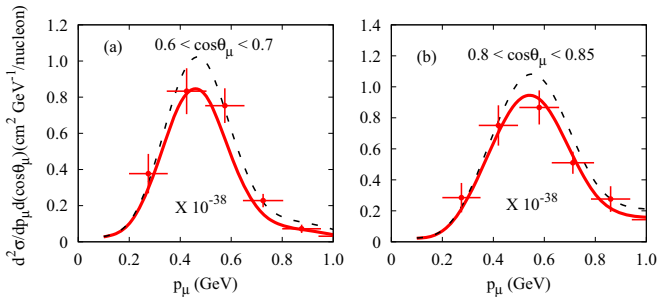

FIG. 9. Double-differential flux-integrated cross section in terms of the incident muon momentum at fixed angle of muon. The experimental data were measured from T2K [10]. Solid (red) curves are the results for $M_A = 1.032$ GeV, and dashed (black) curves are for $M_A = 1.39$ GeV.

cross sections by about 15% from ^{40}Ca and by about 14% from ^{12}C, ^{56}Fe, and ^{208}Pb. From the results of Figs. 4 and 5, the role of M_A is not sensitive to the target nuclei but the contribution of g_A^s increases with heavier nuclei.

In Fig. 6, we calculate the differential cross sections for the CC reaction in terms of the kinetic energies of the knocked-out nucleons from ^{12}C, ^{40}Ca, ^{56}Fe, and ^{208}Pb at the incident neutrino energy of 1.0 GeV. Solid (red) curves are the results for $M_A = 1.032$ GeV and dashed (black) curves are for $M_A = 1.39$ GeV. The effect of M_A enhances the cross sections by about 12% from ^{12}C and ^{40}Ca and by about 15% from ^{56}Fe and ^{208}Pb.

Figure 7 shows the cross sections of the incident antineutrino, and the kinematics are the same as in Fig. 6. The effect of M_A enhances the cross sections by about 5% from ^{12}C and by about 11% from ^{40}Ca, ^{56}Fe, and ^{208}Pb.

For simplicity, we summarize the increasing and decreasing ratios of g_A^s and M_A for different target nuclei at the peak in Tables I and II.

Finally, we compare our results with the MiniBooNE, T2k, and MINERνA experimental data. In Fig. 8, the double-differential cross sections are calculated in terms of the scattering angle $\cos\theta_\mu$ [Figs. 8(a) and 8(b)] and the kinetic energy T_μ [Figs. 8(c) and 8(d)] of the outgoing muon from ^{12}C. The solid lines (red) are the results for $M_A = 1.032$ GeV and the dashed lines are for $M_A = 1.39$ GeV. The solid curves underestimate the experimental data at low T_μ and $\cos\theta_\mu$ but, for higher values of these quantities, they describe the data relatively well. The dashed lines overestimate the data for the higher values but also underestimate the data, especially in Fig. 8(a). According to Figs. 8(a) and 8(b), the peak position shifts toward the right side with higher kinetic energies; that is, the outgoing muon with high kinetic energy passes by the target at a small angle. The peak moves to the right side with smaller scattering angle for the same reason. At the peak, the effect of M_A decreases by about 42% to 35% with higher T_μ [Figs. 8(a) and 8(b)] and decreases by 32% to 26% with larger $\cos\theta_\mu$ [Figs. 8(c) and 8(d)].

Recently, two experiments were performed at T2K and MINERνA whose kinematics are different from the MiniBooNE. In Figs. 9 and 10, we show the double-differential flux integrated cross sections with T2K and MINERνA kinematics. The solid (red) lines are the results for $M_A = 1.032$ MeV and the dashed (black) curves are for $M_A = 1.39$ MeV. Figure 9 shows the cross sections for the muon neutrino versus muon momentum at fixed muon polar angle, and the data were measured from T2K [10]. The kinematics are similar to the MiniBooNE kinematics and then the solid curve describes the T2K experimental data relatively well but the dashed line overestimates the data. The differences between the solid and dashed curves are about 20% for Fig. 9(a) and 15% for Fig. 9(b) around the peak.

In Fig. 10 the double-differential cross sections are shown for the muon antineutrino in terms of the p_T, where $p_\parallel$ and p_T represent the longitudinal and transverse component of the muon with respect to the incoming antineutrino beam, respectively. This kinematics was exploited to include nuclear effects in the neutrino scattering, for which more detailed explanations are available in Ref. [28]. The experimental data were measured from MINERνA [8]. Figures 10(a)–10(c) are the results for $1.5 < p_\parallel < 2.0$, $2.0 < p_\parallel < 2.5$, and $2.5 < p_\parallel < 3.0$ (GeV/c), respectively. The differences between the solid and dashed curves are about 20% for Fig. 9(a) and

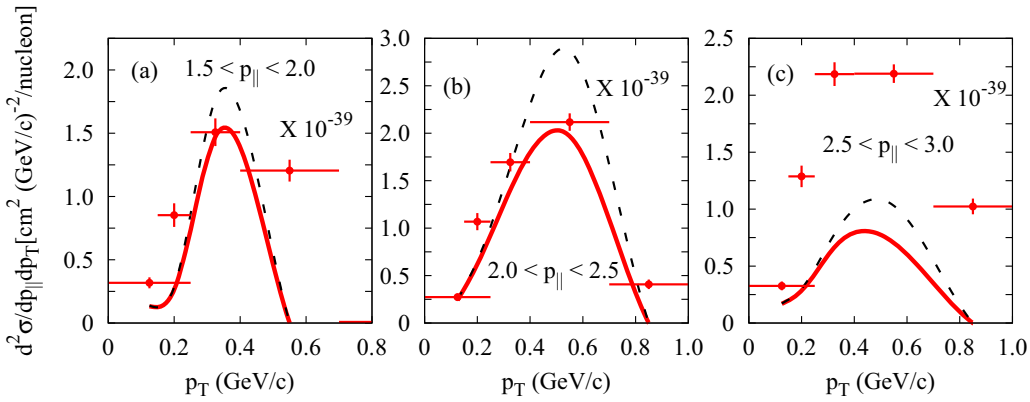

FIG. 10. Double-differential flux-integrated cross section versus muon transverse momentum at fixed muon longitudinal momentum. The experimental data were measured from MINERνA [8]. Solid (red) curves are the results for $M_A = 1.032$ GeV, and dashed (black) curves are for $M_A = 1.39$ GeV.

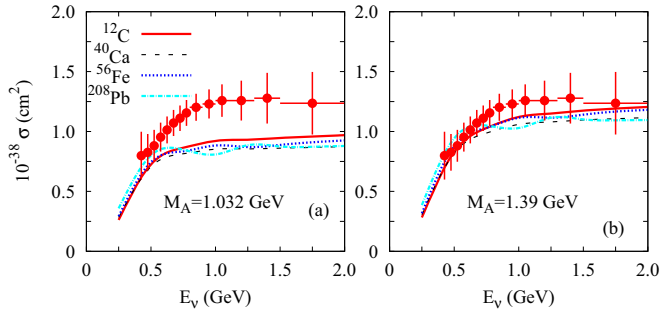

FIG. 11. Total scaled cross sections of the CC ν-A scattering in terms of the incident neutrino energy from ^{12}C, ^{40}Ca, ^{56}Fe, and ^{208}Pb. Solid (red) curves are the results for $M_A = 1.032$ GeV, dashed (black) curves are for $M_A = 139$ GeV, and the data were measured from MiniBooNE [1].

45% for Figs. 10(b) and 10(c) around the peak. Note that the contributions for which the angle of the final muon is greater than 20° are removed according to the MINERνA kinematic restriction. From these results, we learn that the role of M_A is sensitive to the kinematics. Note that our results are similar to those of a recent work [31].

On the other hand, our results do not describe the MINERνA data at all because the momentum of the muon is too large, especially, $p_\parallel > 2.5$ GeV/c. The reason is that the wave functions of the final nucleons are generated by solving the Dirac equation with partial-wave expansion, so a very big angular quantum number for such a large momentum is needed. Unfortunately, within our model, we do not solve the difficulty for such a high momentum of the final nucleon, although we obtained the recipe of this problem for the lepton part with an approximation [27]. Therefore, the result of Fig. 10(c) is not reliable.

In Fig. 11, we calculate the total scaled cross sections in terms of the incident neutrino energies for the CC reaction. The total scaled cross section is the total cross section divided by the number of nucleons which participate in the reaction. For the case of $M_A = 1.032$ GeV, our results underestimate the experimental data by about 25% but for $M_A = 1.39$ GeV our results describe the data well. The effect of the M_A is almost 25% in the total scaled cross section for all four nuclei. Note that the total cross sections are scaled very well.

On the other hand, while we calculate the quasielastic cross section without multinucleon knocked-out processes, there were several works to include the processes like 2p-2h states [32–34]. They found that the 2p-2h states play an important role for the double-differential and total cross sections by comparing with the MiniBooNE data.

IV. SUMMARY

In this paper, we investigate the effects of the strange axial form factor (g_A^s) and axial mass (M_A) for the NC and CC reactions from ^{12}C, ^{40}Ca, ^{56}Fe, and ^{208}Pb nuclei within the framework of a relativistic single-particle model. To investigate the effects, we calculate the differential cross section for the NC and CC reactions and the cross section separately from the proton and the neutron knockouts in the target nucleus. For both proton and neutron knockouts, the effect of M_A enhances the magnitude of the cross sections. It also increases the magnitude of the cross section for the NC and CC reactions about 10%–15% for the all cases except the CC $\bar{\nu}$-^{12}C scattering.

For the case of proton knockout, the effect of g_A^s reduces the cross sections but increases them for the neutron knockout. The effect of g_A^s reduces the cross sections for ^{12}C and ^{40}Ca but it enhances the cross sections for ^{56}Fe and ^{208}Pb because the number of protons and neutrons is the same at ^{12}C and ^{40}Ca but at ^{56}Fe and ^{208}Pb the number of neutrons is more than the number of protons. The role of g_A^s for ^{12}C, ^{40}Ca, and ^{56}Fe is small; about 1%–2%, but is about 5% at heavy nuclei such as ^{208}Pb. From this result, one may deduce that the contribution of g_A^s increases with heavier nuclei, especially with neutron-rich nuclei. Furthermore, according to the comparison of our results with the MiniBooNE, T2K, and MINERνA data (Figs. 8–11), we cannot estimate the value of M_A because the other effects beyond the quasielastic regime such as pion production or 2p-2h contribution are not included.

In conclusion, the effect of M_A is slightly dependent on the target nuclei and is sensitive to the kinematics, but the role of g_A^s increases with heavier nuclei. Furthermore, the dependence on the asymmetry in these targets is not large enough to discuss the effects of the asymmetry in the present calculation, as shown in Tables I and II. The roles of M_A and g_A^s are not sensitive to incident neutrino (antineutrino) energies. In the future, it will be necessary to reproduce the recent experimental data like T2K and MINERνA data with improving our current nuclear model; for example, the effects of nonlinear sigma or chirality will be included.

ACKNOWLEDGMENTS

This work was supported by the National Research Foundation of Korea (NRF) grant funded by the Korea government (MSIT) (Grant No. 2018R1A5A1025563). M.K. Cheoun's work was supported by the National Research Foundation of Korea (Grant No. NRF-2017R1E1A1A01074023 and 2013M7A1A1075764).

[1] A. A. Aguilar-Arevalo *et al.* (MiniBooNE Collaboration), Phys. Rev. D **81**, 092005 (2010).
[2] A. A. Aguilar-Arevalo *et al.* (MiniBooNE Collaboration), Phys. Rev. D **82**, 092005 (2010).
[3] A. A. Aguilar-Arevalo *et al.* (MiniBooNE Collaboration), Phys. Rev. D **88**, 032001 (2013).
[4] A. A. Aguilar-Arevalo *et al.* (MiniBooNE Collaboration), Phys. Rev. D **91**, 012004 (2015).
[5] L. Fields *et al.* (MINERνA Collaboration), Phys. Rev. Lett. **111**, 022501 (2013); G. A. Fiorentini *et al.* (MINERνA Collaboration), *ibid.* **111**, 022502 (2013).
[6] P. A. Rodrigues *et al.* (MINERνA Collaboration), Phys. Rev. Lett. **116**, 071802 (2016).
[7] M. Betancourt *et al.* (MINERνA Collaboration), Phys. Rev. Lett. **119**, 082001 (2017).

[8] C. E. Patrick *et al.* (MINERνA Collaboration), Phys. Rev. D **97**, 052002 (2018).
[9] P. Adamson *et al.* (MINOS Collaboration), Phys. Rev. D **91**, 012005 (2015).
[10] K. Abe *et al.* (T2K Collaboration), Phys. Rev. D **92**, 112003 (2015); **93**, 112012 (2016).
[11] A. Meucci, C. Giusti, and F. D. Pacati, Phys. Rev. D **84**, 113003 (2011).
[12] A. V. Butkevich and D. Perevalov, Phys. Rev. C **84**, 015501 (2011); Phys. Rev. D **89**, 053014 (2014).
[13] M. Martini, M. Ericson, and G. Chanfray, Phys. Rev. C **84**, 055502 (2011).
[14] J. Nieves, I. R. Simo, and M. J. Vicente Vacas, Phys. Rev. C **83**, 045501 (2011).
[15] J. Nieves, I. Ruiz Simo, and M. J. Vicente Vaca, J. Phys.: Conf. Ser. **408**, 012040 (2013).
[16] R. Gonzalez-Jimenez, M. V. Ivanov, M. B. Barbaro, J. A. Caballero, and J. M. Udias, Phys. Lett. B **718**, 1471 (2013).
[17] B. Bhattacharya, G. Paz, and A. J. Tropiano, Phys. Rev. D **92**, 113011 (2015).
[18] J. E. Amaro and E. Ruiz Arriola, Phys. Rev. D **93**, 053002 (2016).
[19] G. D. Megias, M. B. Barbaro, J. A. Caballero, and S. Dolan, Phys. Rev. D **99**, 113002 (2019).
[20] K. S. Kim, Myung-Ki Cheoun, and Byung Geel Yu, Phys. Rev. C **77**, 054604 (2008); K. S. Kim, B. G. Yu, M. K. Cheoun, T. K. Choi, and M. T. Chung, J. Phys. G **34**, 2643 (2007).
[21] K. S. Kim, H. Kim, M.-K. Cheoun, G.-S. Yang, and W. Y. So, Phys. Rev. C **92**, 044613 (2015).
[22] C. Adamuscin, E. Tomasi-Gustafsson, E. Santopinto, and R. Bijker, Phys. Rev. C **78**, 035201 (2008).
[23] L. Alvarez-Ruso, K. M. Graczyk, and E. Saul-Sala, Phys. Rev. C **99**, 025204 (2019).
[24] C. J. Horowitz and B. D. Serot, Nucl. Phys. A **368**, 503 (1981).
[25] K. S. Kim and Myung Ki Cheoun, Phys. Rev. C **67**, 034603 (2003).
[26] K. S. Kim and L. E. Wright, Phys. Rev. C **67**, 054604 (2003).
[27] K. S. Kim, L. E. Wright, Y. Jin, and D. W. Kosik, Phys. Rev. C **54**, 2515 (1996); K. S. Kim, L. E. Wright, and D. A. Resler, *ibid.* **64**, 044607 (2001); K. S. Kim and L. E. Wright, *ibid.* **72**, 064607 (2005); K. S. Kim, B. G. Yu, and M. K. Cheoun, *ibid.* **74**, 067601 (2006).
[28] X. G. Lu *et al.* (MINERνA Collaboration), Phys. Rev. Lett. **121**, 022504 (2018).
[29] K. Abe *et al.* (T2K Collaboration), Phys. Rev. D **98**, 032003 (2018).
[30] K. S. Kim and M.-K. Cheoun, Phys. Rev. C **83**, 034607 (2011).
[31] G. D. Megias, J. E. Amaro, M. B. Barbaro, J. A. Caballero, T. W. Donnelly, and I. Ruiz Simo, Phys. Rev. D **94**, 093004 (2016).
[32] M. Martini, M. Ericson, G. Chanfray, and J. Marteau, Phys. Rev. C **80**, 065501 (2009).
[33] J. Nieves, I. Ruiz Simo, and M. J. Vicente Vaca, Phys. Lett. B **707**, 72 (2012).
[34] I. Ruiz Simo, J. E. Amaro, M. B. Barbaro, A. De Pace, J. A. Caballero, and T. W. Donnelly, J. Phys. G **44**, 065105 (2017).